

The Great Observatories Origins Deep Survey

VLT/VIMOS Spectroscopy in the GOODS-South Field

P. Popesso¹, M. Dickinson⁴, M. Nonino³, E. Vanzella^{2,3}, E. Daddi⁸, R.A.E. Fosbury⁵, H. Kuntschner⁵,
V. Mainieri⁷, S. Cristiani³, C. Cesarsky⁷, M. Giavalisco⁶, A. Renzini², and
the GOODS Team

¹ Max-Planck-Institut für extraterrestrische Physik, Giessenbachstrasse 2, 85748 Garching, Germany

² Dipartimento di Astronomia dell'Università di Padova, Vicolo dell'Osservatorio 2, I-35122 Padova, Italy.

³ INAF - Osservatorio Astronomico di Trieste, Via G.B. Tiepolo 11, 40131 Trieste, Italy.

⁴ National Optical Astronomy Obs., P.O. Box 26732, Tucson, AZ 85726.

⁵ ST-ECF, Karl-Schwarzschild Str. 2, 85748 Garching, Germany.

⁶ Space Telescope Science Institute, 3700 San Martin Drive, Baltimore, MD 21218.

⁷ European Southern Observatory, Karl-Schwarzschild-Strasse 2, Garching, D-85748, Germany.

⁸ Université Paris-Sud 11, Rue Georges Clemenceau 15, Orsay, F-91405, France

⁹ Jet Propulsion Laboratory, California Institute of Technology, MS 169-506, 4800 Oak Grove Drive, Pasadena, CA 91109 *

Preprint online version: October 25, 2018

ABSTRACT

Aims. We present the first results of the VISIBLE Multiobject Spectrograph (VIMOS) ESO/GOODS program of spectroscopy of faint galaxies in the Chandra Deep Field South (CDF-S). The program complements the FORS2 ESO/GOODS campaign.

Methods. 3312 spectra have been obtained in service mode with VIMOS at the ESO/VLT UT3. The VIMOS LR-Blue and MR grisms have been used to cover different redshift ranges. Galaxies at $1.8 < z < 3.5$ have been observed in the GOODS VIMOS-LR-Blue campaign. Galaxies at $z < 1$ and Lyman Break Galaxies at $z > 3.5$ have been observed in the VIMOS MR survey.

Results. Here we report results for the first 6 masks (out of 10 total) that have been analyzed from each of the LR-Blue and MR grisms. Spectra of 2344 spectra have been extracted from these 6 LR-Blue masks and 968 from 6 MR masks. 33% of the LR-Blue and 18% of the MR spectra are serendipitous observations. We obtained 1481 redshifts in the LR-Blue campaign and 656 in the MR campaign for a total success rate of 63% and 68%, respectively, which increase to 70% and 75% when only the primary targets are considered. By complementing our VIMOS spectroscopic catalog with all existing spectroscopic redshifts publicly available in the CDF-S, we created a redshift master catalog. By comparing this redshift compilation with different photometric redshift catalogs we estimate the completeness level of the CDF-S spectroscopic coverage in several redshift bins.

Conclusions. The completeness level is very high, $> 60\%$, at $z < 3.5$, and it is very uncertain at higher redshift. The master catalog has been used also to estimate completeness and contamination levels of different galaxy photometric selection techniques, such as the BzK, the so called 'sub'-U-dropout and the drop-out methods and to identify large scale structures in the field.

Key words. Cosmology: observations – Cosmology: deep redshift surveys – Cosmology: large scale structure of the universe – Galaxies: evolution.

1. Introduction

The Great Observatories Origins Deep Survey (GOODS) is a public, multi-facility project that aims at answering some of the most profound questions in cosmology: how did galaxies form and assemble their stellar mass? When was the morphological differentiation of galaxies established and how did the Hubble

Sequence form? How did AGN form and evolve, and what role do they play in galaxy evolution? How much do galaxies and AGN contribute to the extragalactic background light? A project of this scope requires large and coordinated efforts from many facilities, pushed to their limits, to collect a database of sufficient quality and size for the task at hand. It also requires that the data be readily available to the worldwide community for independent analysis, verification, and follow-up.

The program targets two carefully selected fields, the Hubble Deep Field North (HDF-N) and the Chandra Deep Field South (CDF-S), with three NASA Great Observatories

* Based on observations made at the European Southern Observatory, Paranal, Chile (ESO programme 170.A-0788 *The Great Observatories Origins Deep Survey: ESO Public Observations of the SIRTf Legacy/HST Treasury/Chandra Deep Field South.*)

(HST, Spitzer and Chandra), ESA's XMM-Newton, and a wide variety of ground-based facilities. The area common to all the observing programs is 320 arcmin^2 , equally divided between the North and South fields. For an overview of GOODS, see Dickinson et al. (2003), Renzini et al. (2003) and Giavalisco et al. (2004a).

Spectroscopy is essential to reach the scientific goals of GOODS. Reliable redshifts provide the time coordinate needed to delineate the evolution of galaxy masses, morphologies, clustering, and star formation. They calibrate the photometric redshifts that can be derived from the imaging data at $0.36\text{--}8\mu\text{m}$. Spectroscopy will measure physical diagnostics for galaxies in the GOODS field (e.g., emission line strengths and ratios to trace star formation, AGN activity, ionization, and chemical abundance; absorption lines and break amplitudes that are related to the stellar population ages). Precise redshifts are also indispensable to properly plan for future follow-up at higher dispersion, e.g., to study galaxy kinematics or detailed spectral-line properties.

The ESO/GOODS spectroscopic program is designed to observe all galaxies in the CDF-S field for which VLT optical spectroscopy is likely to yield useful data. The program is organized in two campaigns, carried out at VLT/FORS2 at UT1 and VLT/VIMOS at UT3. The program makes full use of the VLT instrument capabilities, matching targets to instrument and disperser combinations in order to maximize the effectiveness of the observations.

The FORS2 campaign is now completed (Vanzella et al. 2005, 2006, 2008). 1715 spectra of 1225 individual targets have been observed and 887 redshifts have determined as a result. Galaxies have been selected adopting three different color criteria and using the photometric redshifts. The resulting redshift distribution typically spans two redshift domains: from $z = 0.5$ to $z = 2$ and $z = 3$ to $z = 6.5$. The reduced spectra and the derived redshifts are released to the community through the ESO web page <http://www.eso.org/science/goods/>. The typical redshift uncertainty is estimated to be $\sigma_z \sim 0.001$.

We are currently conducting the VIMOS ESO/GOODS spectroscopic survey to complement the FORS2 survey in terms of completeness and sky coverage. The cumulative source counts on the CDF-S field taken from the deep public FORS1 data (Szokoly et al. 2004), show that down to $V_{\text{AB}} = 25 \text{ mag}$ there are 6000 objects over the 160 arcmin^2 of the GOODS field. Only the high multiplexing capabilities of VIMOS at VLT can ensure to reach the required completeness in a reasonable amount of time. On average ~ 330 objects at a time have been observed with the low resolution ($R \sim 250$) grism and ~ 140 with the medium ($R \sim 1000$) grism.

A Medium resolution campaign in the red (VIMOS MR orange grism) is designed to reach the required completeness in the $0.5 < z < 1.3$ and $z > 3.5$ redshift ranges. A low resolution spectroscopic campaign is conducted with the VIMOS LR-Blue grism to cover the $1.8 < z < 3.5$ redshift range not covered by the FORS2 spectroscopy. The aim is to reach $\text{mag} \sim 24\text{--}25$ with adequate S/N, with this limiting magnitude being in the B band for objects observed with the VIMOS LR-Blue grism, in the R band for those observed in the VIMOS MR-Orange grism, and in the z band for the objects observed with FORS2.

In this paper we report on the first 60% of the VIMOS spectroscopic follow-up campaign in the Chandra Deep Field South (CDF-S), carried out with the VIMOS instrument at the ESO VLT from P74 to P78. 10 masks have been observed in the LR-Blue grism and 10 with the MR Orange grism. Here we report results for the first 6 masks that have been analyzed from each of the LR-Blue and MR grisms.

The paper is organized as follows: in Sect. 2 we describe the survey strategy and in Sect. 3 the observations and the data reduction. The details of the redshift determination is presented in Sect. 4. In Sect. 5 we discuss the data and in Sect. 6 the reliability of the photometric techniques used to identify the high redshift targets. In Sect. 7 we present our the conclusions. Throughout this paper the magnitudes are given in the AB system ($AB \equiv 31.4 - 2.5 \log(f_\nu/nJy)$), and the ACS F435W, F606W, F775W, and F850LP filters are denoted hereafter as B_{435} , V_{606} , i_{775} and z_{850} , respectively. We assume a cosmology with $\Omega_{\text{tot}}, \Omega_M, \Omega_\Lambda = 1.0, 0.3, 0.7$ and $H_0 = 70 \text{ km s}^{-1} \text{ Mpc}^{-1}$.

2. The survey strategy

2.1. The VIMOS instrument

The Visible MultiObject Spectrograph (VIMOS) is installed on the ESO/VLT, at the Nasmyth focus of the VLT/UT3 'Melipal' (Le Fevre et al. 2003). VIMOS is a 4-channel imaging spectrograph, each channel (a 'quadrant') covering $\sim 7 \times 8 \text{ arcmin}^2$ for a total field of view (a 'pointing') of $\sim 218 \text{ arcmin}^2$. Each channel is a complete spectrograph with the possibility to insert slit masks $\sim 30 \times 30 \text{ cm}^2$ each at the entrance focal plane, broad band filters or grisms to produce spectra on $2048 \times 4096 \text{ pixels}^2$ EEV CCD.

The pixel scale is $0.205 \text{ arcsec/pixel}$, providing excellent sampling of the Paranal mean image quality and Nyquist sampling for a slit of 0.5 arcsec in width. The spectra resolution ranges from ~ 200 to ~ 5000 . Because the instrument field at the Nasmyth focus of the VLT is large ($\sim 1 \text{ m}$), there is no atmospheric dispersion compensator. This requires the observer to limit observations to airmasses below 1.1.

In the MOS mode of observations, short 'pre-images' are taken ahead of the observing run. These are cross-correlated with the user-catalog to match the instrument coordinate system to the atmospheric reference of the user catalog. User masks are, then, prepared using the VMMP tool, provided by ESO, with an automated optimization of slit number and position (see Bottini et al. 2005).

2.2. The Field coverage: VIMOS pointing layout

The VIMOS geometry ($16' \times 18'$, with a cross gap of $2'$ between the quadrants) is such that only 50% of it can overlap with the $10' \times 16'$ GOODS-CDFS field. At least 3 VIMOS pointings are required to cover the whole GOODS area (see Fig. 1). The VIMOS multiplex allows measurement of an average of ~ 360 per pointing in the case of the Low Resolution (LR) grism and ~ 150 in the case of the Medium Resolution (MR) grism. 10 Low resolution and 10 Medium Resolution masks (on average 3 LR and 3 MR masks per pointing) are

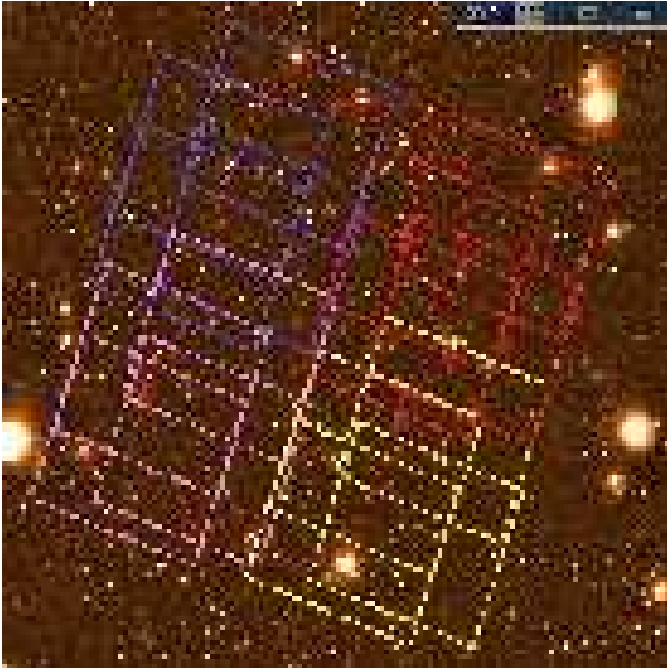


Fig. 1. VIMOS field coverage of the GOODS area in the CDF-S.

necessary to ensure $\sim 96\%$ completeness in the spectroscopic coverage of ~ 6000 targets. With an average integration time of 4h per mask and 30% overheads, this makes a total of 125h.

2.3. Target Selection

Several categories of object selection criteria have been used to ensure a sufficiently high density of target candidates on the sky to efficiently fill out multi-slit masks. The target selection is based on the multiwavelength photometry available for the GOODS-S field. Different criteria have been used for the low resolution 'LR-Blue' grism and the medium resolution 'MR Orange' grism. In both part of the GOODS VIMOS survey the selection criteria and the target catalog have been tailored in time to optimize the survey success rate. The target catalog have been changed according to the incoming new GOODS dataset: partial results of the spectroscopic surveys, updated GOODS photometric catalogs, Spitzer IRAC and MIPS data. Moreover, the VIMOS quadrants cover an area larger than the GOODS field. Thus, different datasets have been used to create the target catalogs of the GOODS field and the remaining area. We summarize here the main criteria of selection used during the GOODS VIMOS survey in ESO observing periods P74-P78.

The VIMOS LR-Blue grism covers the wavelength range $3500 - 6900 \text{ \AA}$. Hence it is suitable for the observation of the ultraviolet absorption and emission features of objects in the redshift range $1.8 \leq z \leq 3.8$. The target selection of the low resolution campaign is based on the following criteria:

- U-dropouts: CTIO and WFI photometry based U-drops (see Section 6 and Lee et al. 2006 for the detailed description of the selection criteria)
- BzK color-selected objects with IRAC color preselection (when available) to favor $z \sim 2$ galaxies (Daddi et al. 2004)
- “so-called” sub-U-dropouts: color-selected objects with *UBR* colors falling below of those of normal $z \sim 3$ Lyman break color selection criteria, similar to 'BX' selection criterion of Adelberger et al. (2004, see Section 6 for the detailed description of the selection criteria). Sub-U-dropouts selection criteria are based on CTIO U-band and WFI photometry.
- X-ray sources from the CDF-S and E-CDF-S X-ray catalogs (Giacconi et al. 2002, Lehmer et al. 2005)

No low redshift galaxies have been targeted for the LR-Blue masks. A magnitude cut at $B < 24.5$ mag is applied to all target catalogs listed above.

The wavelength range of the VIMOS MR Orange grism is $4000 - 10000 \text{ \AA}$, similarly to FORS2. However, the fringing at red wavelength ($\lambda \geq 7000 \text{ \AA}$) is somewhat stronger than in FORS2. Hence, the optical spectral emission and absorption features for galaxies at $z > 1$, and the ultraviolet spectral features of Lyman break galaxies (LBG) at $z \gtrsim 4.8$, which would appear at very red optical wavelengths, are not well detectable. Therefore, the target selection is limited to bright galaxies and LBGs in the redshift range $2.8 < z < 4.8$. The selection is based, as for the LR-Blue campaign, on the available photometry according to the following criteria:

1. galaxies at $R < 24.5$ with the exclusion of VIMOS LR-Blue targets and objects already observed.
2. MIPS selected targets $R < 24.5$ mag with the exclusion of VIMOS LR-Blue targets and objects already observed.
3. faint Lyman break galaxies at $i_{775} < 25$, selected as B_{435} , V_{606} dropouts.

When designing the masks, we avoid as much as possible to observe targets that had already been observed in other redshift surveys of this field, namely, the K20 survey of Cimatti et al. (2002), the survey of X-ray sources by Szokoly et al. (2004), the VIMOS VLT Deep Survey (Le Fevre et al. 2005) and the ESO/GOODS FORS2 survey (Vanzella et al. 2005, 2006).

3. Observations and Data Reduction

The VLT/VIMOS spectroscopic observations were carried out in service mode during ESO observing periods P74-P78.

3.1. Preparation of VIMOS observations

For each pointing a short V-band image is taken with VIMOS ahead of the spectroscopic observations. We used the preimaging together with the GOODS WFI R band image to derive the transformation matrix from the (α, δ) sky reference frame of the target catalogs to the (X_{CCD}, Y_{CCD}) VIMOS instrumental coordinate system. The cross-correlation is performed with

the routines *geomap* and *geoxytran* in the IRAF environment, which turn out to reach a spatial accuracy, ~ 0.05 arcsec, ten times higher than the accuracy of the matching procedure implemented in the VIMOS mask preparation software (VMMPS, Bottini et al. 2005). This is due to the choice of a higher order polynomial of the fitting procedure, which is not allowed in VMMPS. Once the target catalog is expressed in the (X_{CCD}, Y_{CCD}) VIMOS instrumental coordinate system, the next steps are conducted with VMMPS tool, to design the slit mask layout. After placing two reference apertures on bright stars for each pointing quadrant, slits are assigned to a maximum number of sources in the photometric catalog. The automated SPOC (Slit Positioning Optimization Code, Bottini et al. 2005) algorithm is run to maximize the number of slits given the geometrical and optical constraints of the VIMOS set-up. We have designed masks with slits of one arcsec width, and have forced that a minimum of 1.8 arcsec of sky is left on each side of a targeted object to allow for accurate sky background fitting and removal during later spectroscopic data processing. On average, taking advantage of the VIMOS multiplexing capability, a GOODS pointing of 4 quadrants LR-Blue mask contains up to 360 slits. Masks with the VIMOS MR grism were designed with a multiplexing of 1 to avoid the superposition of zero and negative orders between adjacent spectra. Thus, a pointing of 4 quadrants MR mask can contain, on average, 150 slits. Dithering of the targets along the slits was applied in order to effectively improve the sky subtraction and the removal of CCD cosmetic defects. In the LR-Blue survey, the dithering pattern consisted of three positions separated by a step of 1.4 arcsec. In the MR survey, the dithering pattern consisted of five positions separated by a step of 1.5 arcsec, in order to provide enough independent pointings to construct and apply a correction for fringing at red wavelengths (see section 3.2).

In the LR-Blue campaign, we have used the LR-Blue grism together with the OS-Blue cutoff filter, which limits the bandpass and order overlap. With 1 arcsec slits, the resolution is $\sim 28 \text{ \AA}$ and the dispersion is 5.7 \AA/pixel . 10 exposures of 24 minutes each are taken for a total exposure time of 4h per mask. In the MR campaign, the MR Orange grism is used together with the GG475 filter. With 1 arcsec slits, the resolution is $\sim 13 \text{ \AA}$ and the dispersion is 2.55 \AA/pixel . 12 exposures of 20 minutes each are taken for a total exposure time of 4h per mask. We have asked for night arc-lamp calibration to reduce problem due to the instrument instability.

3.2. Data Reduction

The pipeline processing of the VIMOS-GOODS data is performed using the VIMOS Interactive Pipeline Graphical Interface (VIPGI, see Scodreggio et al. 2005 for a full description). The data reduction is performed in several interactive steps: the spectra location in the individual spectroscopic frames, the wavelength calibration, sky subtraction and fringing correction, combination of the 2D spectra of dithered observations, extraction of the 1D spectra and flux calibration. The location of the slits is known from the mask design process, hence, knowing the grism zero deviation wavelength and the

dispersion curve, the spectra location is known a priori on the detectors. However, small shifts from predicted positions are possible due to the complete manufacturing and observation process. From the predicted position, the location of the spectra are identified accurately on the 4 detectors and an extraction window is defined for each slit. The wavelength calibration is secured by the observation of night arc-lamps through the observed mask. Wavelength calibration spectra are extracted at the same location as the object spectra and calibration lines are identified to derive the pixel to wavelength mapping for each slit. The wavelength to detector pixel transformation is fit using a third order polynomial, resulting in a median rms residual of $\sim 0.7 \text{ \AA}$ across the wavelength range in the LR-Blue masks and $\sim 0.36 \text{ \AA}$ in the MR masks. A low order polynomial (second order) is fit along the slit, modeling the sky background contribution at each wavelength position, and subtracted from the 2D spectrum. In the case of the LR-Blue campaign the fringing is not present and all 10 exposures of a sequence are directly combined by shifting the 2D spectra following the offset pattern to register the object at the same position. The individual frames are combined with a median, sigma-clipping algorithm to produce the final summed, sky subtracted 2D spectrum. In the case of the Medium resolution spectra, the fringing is significant at $\lambda > 7000 \text{ \AA}$ and needs to be removed. Therefore, a fringing correction is applied before combining the dithered frames. As the object is moved to different positions along the slit following the effect pattern, the median of the 2D sky subtracted spectra produces a frame from which the object is eliminated, but that includes all residuals not corrected by sky subtraction, in particular the fringing pattern varying with position across the slit and wavelength. This sky/fringing residuals is, then, subtracted from each individual 2D sky subtracted frame. The fringing corrected frames are, then, combined as in the case of the LR-Blue spectra.

The last step done automatically by VIPGI is to extract a 1D spectrum from the summed 2D spectrum, using an optimal extraction following the slit profile measured in each slit (Horne, 1986). The 1D spectrum is flux calibrated using the ADU to absolute flux transformation computed from the observations of spectrophotometric standard stars.

A final check of the 1D calibrated spectra is performed and the most discrepant features are removed manually, cleaning each spectrum of zero order contamination, sky lines residuals and negative non physical features.

3.3. The VIMOS LR-Blue wiggles

Spurious wiggles of amplitude of about 3 to 8% have been detected in VIMOS MOS spectra taken with the combination of LR-Blue grism and OS-Blue Order Sorting (OS) filter. The position of the wiggles in the spectrum compares well with the wiggles in the response curve of the OS-Blue filter (see also the ESO VIMOS User Manual, fig. A.3). This clearly indicates that the wiggles originate in the OS filter. As such, then, the effect of the wiggles is multiplicative. In principle, spectroscopic screen flat-fields, even taken during the day, would be sufficient to correct the wiggles. However, several aspects make this cor-

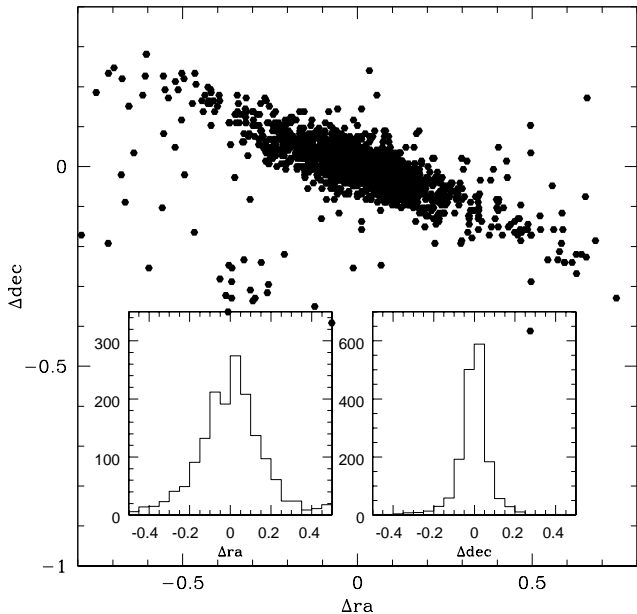


Fig. 2. Δra and Δdec residual distribution of the cross-correlation between “reconstructed” WFI coordinates and original target coordinates. The strong distortion of VIMOS quadrants is not completely removed as indicated by the trend in the Δra - Δdec distribution shown in the main panel. However, the rms of the cross-correlation is lower than 0.2 arcsec in both coordinates, as shown by the Δra and Δdec histograms in the smaller panels, ensuring an accurate target identification.

rection very difficult. The wiggles position and amplitude are found to depend on the spectral resolution, which in turn depends on slit width and object size. The wiggle pattern and the overall shape of the flat field spectra depend significantly on the position of the slit in the field of view. In addition, The normalization of flat field spectra is made problematic by the possible overlap of 0th order spectra from neighboring slits. For these reasons we prefer not to correct the wiggles observed in the LR-Blue spectra.

3.4. Target coordinates

Due to the rotation angle of the VIMOS GOODS pointings (-20 deg), which is different from the default values accepted by VIPGI (0 and 90 deg), VIPGI does not provide the astrometry of the extracted spectra. The only information provided by VIPGI are the coordinates in mm on the focal plane stored in the so called VIPGI *object table*. To overcome this problem, we transform the focal plane coordinates of each object into CCD coordinates through the appropriate distortion map stored in the header of our VIMOS observations. Slits which contain only one object (only one spectrum extracted) are used to calculate the transformation matrix from VIMOS to the GOODS R-band WFI CCD coordinates through the IRAF routines *geomap* and *geoxytran*. As a last step the WFI X_{CCD} and Y_{CCD} assigned to each extracted spectrum are converted to α , δ on the basis

of the WFI-GOODS astrometry. These ‘reconstructed’ coordinates are, then, matched to the original GOODS VIMOS target catalog to identify the primary targets and the serendipitous objects. After the identification, the original WFI target coordinates are assigned to the primary targets while the secondary objects keep the reconstructed coordinates. Fig. 2 shows the distribution of the Δra and Δdec in the cross-correlation of the reconstructed WFI coordinates and the original targets coordinates. The very strong distortion of the VIMOS CCD is not completely removed as indicated by the trend in the Δra - Δdec distribution shown in the main panel. This is due to the fact that we can use few objects to calculate the transformation matrix from VIMOS to the GOODS R-band WFI CCD coordinates. However, the rms of the cross-correlation is lower than 0.2 arcsec in both coordinates (see the Δra and Δdec histograms in the smaller panels of the same figures), allowing for an accurate target identification.

It is worth to mention that due to a bug, VIPGI assigns wrong focal plane coordinates to a small sample of objects in slits with more than 2 spectra. We identify 82 cases in the LR-Blue campaign, of which 80% has no redshift determination, and 34 in the MR campaign, of which 50% has no redshift determination. Those objects have focal plane coordinates $x_{fp} = 0.0, y_{fp} = 0$. Moreover, on the basis of the reconstructed WFI coordinates these objects are located completely out of the slit where they should be. The complete list of those objects is available at <http://www.eso.org/science/goods/>.

4. Redshift Determination

2344 spectra have been extracted from the 6 LR-Blue masks and 968 have been extracted from 6 MR masks. From them we have been able to determine 1481 redshifts in the LR-Blue campaign and 656 in the MR campaign. 33% of the LR-Blue slits and 18% of the MR slits contain more than one spectrum. Most of the secondary spectra obtained provide additional observations of known targets. We have identified 2235 unique LR-Blue objects and 886 unique MR sources.

In the large majority of the cases the redshift has been determined through the identification of prominent features of galaxy spectra:

- at low redshift the absorption features: the 4000Å break, Ca H and K, H δ and H β in absorption, g-band, MgII 2798
- and the emission features: [O II]3727, [O III]5007, H β , H α
- at high redshift: Ly α , in emission and absorption, ultra-violet absorption features such as [Si II]1260, [O I]1302, [C II]1335, [Si IV]1393,1402, [S II]1526, [C IV]1548,1550, [Fe II]1608 and [Al III]1670

The redshift estimation has been performed cross-correlating the individual observed spectra with templates of different spectral types: S0, Sa, Sb, Sc, EII. for the low redshift spectra, several Lyman break galaxies templates in absorption and emission, BzK and AGN template. The cross-correlation is performed by using the *rvsao* package (*xcsao* routine) in the IRAF environment on each spectrum. In particular, an error and trial approach is used for the $z > 1.8$ galaxies, whose redshift

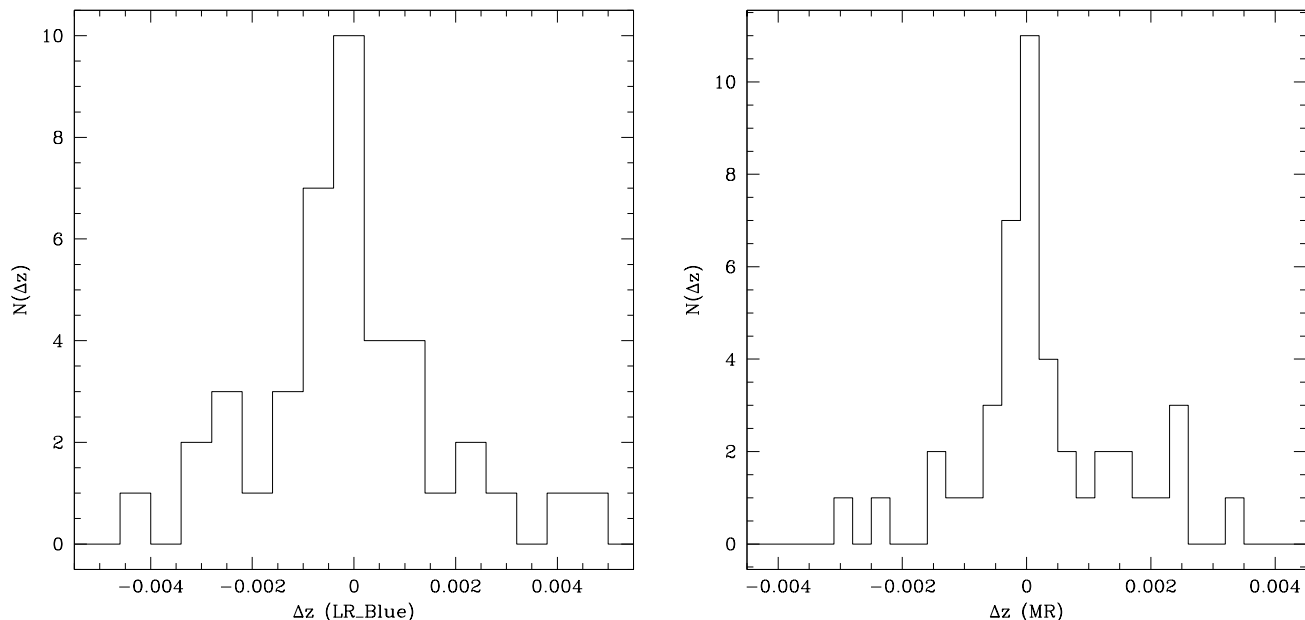


Fig. 3. Redshift differences between objects observed twice or more in independent VIMOS LR-Blue (left panel) and MR (right panel) observations. The distribution has a dispersion of $\sigma_z = 0.0013$ in the LR-Blue campaign and $\sigma_z = 0.0007$ in the MR campaign.

determination is made difficult by the low S/N spectral absorption features and the wiggles in the LR-Blue spectrum.

In analogy to the complementary GOODS-FORS2 redshift campaign, we use four quality flags to indicate the quality of each redshift estimation. The determination of the quality flag is done in two steps. As a first step, the assignment of the quality flag is done during the cross-correlation of the spectrum with the templates on the basis of the cross-correlation coefficient provided by the routine *xcsao* in the IRAF environment. The quality flags are assigned with the following criteria:

- flag A: high quality, values of the *xcsao* correlation coefficient $R \geq 5$; emission lines and strong absorption features are well identified.
- flag B: intermediate quality, values of the *xcsao* correlation coefficient $3 \leq R < 5$; one emission line plus few absorption features are well identified.
- flag C: low quality, values of the *xcsao* correlation coefficient $R < 3$, features of the continuum not well identified.
- flag X: no redshift estimated, no features identified.

As a second step, each spectrum with the superposed main spectral features, is checked by eye by different people and a refinement of the redshift determination and the quality flag assignment is performed. On average, each spectrum is checked more than three times.

In $\sim 15\%$ of the cases the redshift is based only on one emission line, usually identified with [O II]3727 or Ly α . In these cases the continuum shape, the presence of breaks, the absence of other spectral features in the observed spectral range and the broad band photometry are particularly important in the evaluation. In general these solo-emission line redshifts are

classified as “likely” (B) or “tentative” (C) if the no other information are provided by the continuum.

The internal redshift accuracy can be estimated from a sample of galaxies which have been observed twice in independent VIMOS mask sets. We find 39 of such objects in the LR-Blue masks and 40 in the MR masks with quality flag A and B. $\sim 45\%$ of this objects have been observed as serendipitous objects. The distribution of measured redshift differences is presented in Figure 3. The mean of the LR-Blue (left panel of the figure) and the MR (right panel of the figure) Δz distribution is close to zero ($\sim 10^{-5}$) in both cases. The redshift dispersion is $\sigma_z = 0.0013$ ($\sim 400 \text{ km s}^{-1}$) for the LR-Blue objects and $\sigma_z = 0.0007$ ($\sim 200 \text{ km s}^{-1}$) for the MR redshifts. This latter estimation is in very good agreement with the value obtained in the GOODS-FORS2 survey (Vanzella et al. 2005), conducted on similar objects using similar spectral resolution and spectral range as VIMOS MR. We note that the mean values of the redshift estimation uncertainty estimated in this way are ~ 3 times larger than the mean error ($\sigma_z = 0.0004$ in the LR-Blue survey and $\sigma_z = 0.0002$ in the MR survey) calculated by the IRAF routine *xcsao*.

4.1. The success rate

We measured a redshift for 63% (70% for the primary targets) of the observed LR-Blue spectra. However, to estimate the success rate of the surveys we use only the objects with high quality flags, A and B. In the LR-Blue survey the success rate is 39% if we consider the whole sample and 48% if we consider only the primary targets. The serendipitous sources, which account for 33% of the sample, are usually faint neighbor and

Table 1. Success rate of the GOODS VIMOS LR-Blue campaign. The first column lists the name of the target family, the second column lists the fraction of the target catalog due to the corresponding color selection (BzK and sub-udrpout family overlap largely but they are considered as separated family in the table). The third column lists the success rate (fraction A+B flag objects) of each target family. The last four columns list the percentage of A, B, C and X flag redshift determinations, respectively.

Target	fraction	s.r.	A	B	C	X
U-dropouts	16%	49%	35%	14%	15%	36%
BzK	51%	36%	24%	12%	21%	43%
sub-U-dropouts	66%	51%	35%	16%	16%	33%
X-ray	5%	51%	37%	14%	14%	35%

lie often at the edge of the 2D spectrum. For these objects the success rate is very low, $\sim 20\%$. We have investigated how the success rate depends on the target selection and on the redshift windows. As described in Sec. 2.2, the LR-Blue targets can be divided in 4 families: U-dropouts, BzK objects, sub-udropouts and X-ray sources. BzK and sub-udropouts samples largely overlap. In this discussion we consider the two family individually. Table 1 shows the fraction of targets observed in the analyzed masks and the corresponding success rate for each target family. The BzK objects have the lowest success rate. 64% of those objects have flag C or no redshift (flag X) leading to a very low success rate. All the other target families have a success rate of $\sim 51\%$. In addition we find a strong dependence of the success rate on the redshift window. In particular:

- the objects at low redshift ($z_{spec} < 1$) and in the range $2.2 \leq z_{spec} \leq 3.5$ have the highest fraction of A flags, $\sim 60\%$
- the very high redshift galaxies ($z_{spec} > 3.5$) have mainly quality flag B because the Ly α in emission is in the very red part of the spectrum and the other features are not well identified
- the objects at $1.8 < z_{spec} < 2.2$ show the highest fraction of insecure redshift determinations (percentage of the C flag determination $\sim 65\%$)

There are two main reasons for the high failure rate at redshift $1.8 < z_{spec} < 2.2$ and for the BzK galaxies, which lie mainly in this redshift range. The first one is that the Ly α is generally outside the spectral range covered by the LR-Blue grism, at $\lambda < 3600\text{\AA}$. Therefore, other ‘secondary’ spectral features, such as SII, OI, CII, SiIV, SII, and CIV, have to be used to estimate the redshift. However, these features are not as strong as the Ly α in absorption or emission. In addition, at $\lambda < 4000\text{\AA}$ the VIMOS efficiency drops very quickly and the presence of the wiggles described in Sec.3.3, makes the redshift determination very insecure. In fact, only for the very bright sources the S/N at $\lambda < 4000 - 4200\text{\AA}$ is high enough to identify the ‘secondary’ features of the continuum.

We measured a redshift for 67% (75% for the primary targets) of the observed MR spectra. In the VIMOS MR campaign the overall success rate (A+B flag redshifts) is 60% and reaches

the 65% level if only the primary targets are considered. We do not note any dependence on the target selection criteria and redshift windows.

5. Discussion

5.1. Reliability of the redshifts - comparison with previous surveys

A practical way to assess the reliability of the redshifts is to compare the present results with independent measurements of other surveys. For this purpose we use the results of four surveys conducted on the same field: the GOODS-FORS2 campaign (Vanzella et al. 2005, 2006, 2008), the K20 survey (Cimatti et al. 2002), Szokoly et al. (2004) and the VVDS survey (Le Fevre et al. 2005). To create a secure redshift reference sample, we have selected only the high quality redshift determinations of those surveys: GOODS FORS2 quality A and B, K20 quality 1, VVDS quality 3 and 4 and Szokoly et al. 2004 quality 3 and 2+ redshifts, which have all a confidence higher than 95%).

Among the LR-Blue redshift determinations, there are 113 VIMOS objects in common with this high quality reference sample within a spatial accuracy of 0.5 arcsec or better. 58 of them have VIMOS quality flag A, 16 have flag B, 16 have flag C and 23 do not have a redshift estimation (flag X). These 23 objects lie in a redshift range, $0.8 < z < 1.7$, not accessible to VIMOS LR-Blue. 27 cases of the A,B and C quality redshifts show ‘catastrophic’ discrepancies ($|z_{VIMOS} - z_{FORS2/K20/VVDS}| > 0.015$), which account for 5 of the VIMOS flag A objects, 8 of the flag B and 11 of the flag C sources.

After visual comparison of the VIMOS and FORS2/K20/VVDS/CDF spectra we find that 3 of the 5 VIMOS flag A spectra showing ‘catastrophic’ discrepancies are wrong VIMOS redshift determinations.

- VIMOS GOODS_LRb_001_q2_1_1 versus FORS2 GDS_J033217.78-274823.8: the [OIII] in emission is identified in the FORS2 spectrum and it is hidden by a strong sky line residual in the VIMOS spectrum. Thus, the [OII] in the VIMOS spectrum is missclassified as Ly α
- VIMOS GOODS_LRb_001_1_q1_51_1 versus FORS2 GDS_J033226.67-274013.4: the [OII] in the FORS2 spectrum is identified at $z=1.612$, a redshift window not accessible to VIMOS LR-Blue. No emission lines are visible in the VIMOS spectrum and the low S/N UV absorption features are missclassified.
- VIMOS GOODS_LRb_001_q2_35_1 versus VIMOS LR-Red VVDS 32126: the strong UV absorption features identified in the VIMOS spectrum provide a *xcsao* correlation coefficient similar to that of the FeII and NeV absorption features identified in the VVDS spectrum. We have combined the two spectra and re-performed the cross correlation. The highest correlation peak corresponds to the VVDS redshift estimation.
- VIMOS GOODS_LRb_001_q3_71_2 versus VIMOS LR-Red VVDS 16975: the VIMOS LR-Blue source is an emission line galaxy and the reference VVDS spectrum is

clearly an early type galaxy without any emission line. The two spectra can not refer to the same object. Since 16975 is a secondary object and not a primary target, we suspect that the coordinates provided by VIPGI (used to reduce the VVDS data) could be wrong as explained in Sec. 3.4. Thus, we consider the VIMOS redshift estimation correct.

- VIMOS GOODS_LRb_002_q2_55_1 versus FORS2 GDS_J033221.94-274338.8: the strong emission line in the VIMOS spectrum is identified as $\text{Ly}\alpha$ due to the absence of $\text{H}\beta$ and $[\text{OIII}]$ emissions and due to the photometry (the target is a U-drop-out). If something, the emission could be classified as a $[\text{OII}]$ at much lower redshift ($z=0.166$) with a much lower *xcsao* correlation coefficient. In both cases the FORS2 redshift is not in agreement. We have combined the two spectra and re-measured the redshift. The correlation gives a good result only with a $\text{Ly}\alpha$ emitter template at $z=2.576$. No match is found for the emission seen in the FORS2 spectrum which has a very low S/N. We think that the line identified as $[\text{OII}]$ in the FORS2 spectrum is instead due to a fringing residual since it is sitting on a sky line. Thus, we consider the VIMOS redshift estimation correct.

The resulting confidence level in the flag A redshift determinations is 95% (3 mistakes out of 58 redshift determinations). Among the flag B spectra showing ‘‘catastrophic’’ discrepancies, 6 VIMOS redshift determinations are wrong mainly due to the presence of sky residuals and 0th order of neighboring spectra, and only 2 are more convincing than the FORS2/K20/VVDS/CDF determinations. The resulting confidence level is 62% (6 mistakes out of 16 redshift determinations). In all the Flag C discrepancies cases the FORS2/K20/VVDS/CDF redshift determinations are more convincing than the LR-Blue identified ultraviolet features. The resulting confidence level is 31%. However, it is important to note that the VIMOS flag C is assigned in the majority of the cases to redshifts in the range $1.8 < z < 2.2$ as explained in Sec. 4.1. The redshift surveys considered in this comparison (FORS2, K20, VVDS and CDF) are not designed to cover this redshift range. Thus, such comparison can only reveal the mistakes and can not provide confirmations to our estimates. In conclusion, 19 redshift determinations out of 90 are wrong resulting in an overall confidence level of 78% in the LR-Blue VIMOS redshifts. For the 71 cases out of 90 which show good agreement, we find a mean difference $\langle z_{\text{LR-Blue-VIMOS}} - z_{\text{FORS2/K20/VVDS}} \rangle = 0.0018 \pm 0.0019$, which confirms the mean uncertainty Δz found in Sec. 4.

The comparison between the VIMOS MR redshift determinations and FORS2/K20/VVDS/CDF values is simplified by the fact that the MR survey is very similar in design to the considered surveys. There are 94 VIMOS objects in common with the high quality reference sample within a spatial accuracy of 0.5 arcsec. 69 of them have VIMOS quality flag A, 17 have quality flag B and 8 have quality flag C. We find 5 ‘‘catastrophic’’ discrepancies: 1 of them have flag A, 1 have flag B and 3 have flag C:

- flag A case GOODS_MR_new_1_d_q3_22_1 versus FORS2 GDS_J033243.19-275034.9: an accurate analysis is pro-

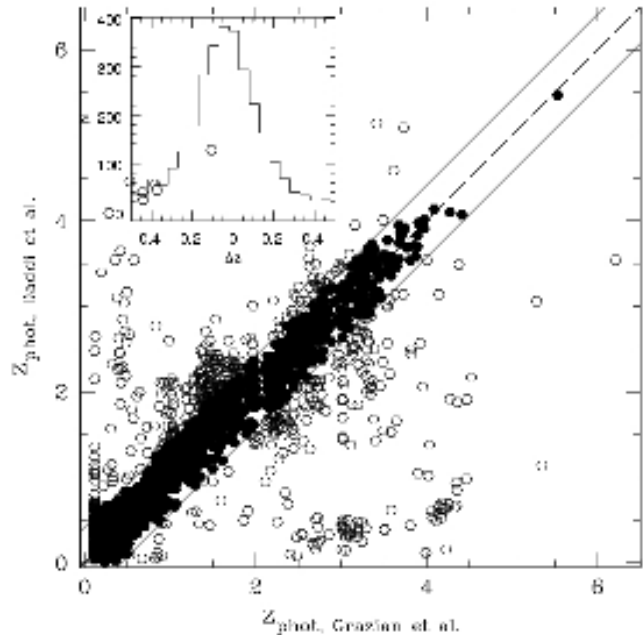


Fig. 4. Comparison of the GOODS-MUSIC and the GOODS photometric redshift catalog. The dashed line shows the slope 1 line and the solid lines show the 3σ limits. The small panel within the main frame shows the $\Delta z = z_{\text{MUSIC}} - z_{\text{GOODS}}$ distribution with $\sigma = 0.13$.

vided by Vanzella et al. (2006, see their Figure 2). The continuum shows increasing bumps/bands in the red, very similar to typical cold stars. After visual inspection of the ACS color image Vanzella et al. 2006 concluded that GDS_J033243.19-275034.9 is a simultaneous spectrum of two very close sources: a star and a possible high- z galaxy.

- B flag case VIMOS GOODS_MR_new_1_d_q3_22_1 versus FORS2 GDS_J033249.04-2705015.5: the spectral features used for the identification are all at $\lambda > 7500$, where the fringing is very strong. The corresponding FORS2 spectra, which suffer less of fringing, show more convincing spectral features.

In the 3 flag C cases, the FORS2/K20/VVDS/CDF redshift estimates seem to be more robust than the VIMOS redshifts. In all three cases the spectral features used to identify the redshift are in the region strongly affected by fringing.

Thus, we obtain a confidence level of 98% for the quality A MR redshifts (1 mistake out of 69 redshifts), 94% for the quality B redshifts (1 mistakes out of 17 determinations) and 62% for the quality C cases (3 mistakes out of 8 determinations). The overall confidence level of the redshift determinations of the MR redshift survey is 95%. For the 89 cases out of 94 which show good agreement, we find a mean difference $\langle z_{\text{MR-VIMOS}} - z_{\text{FORS2/K20/VVDS}} \rangle = 0.0013 \pm 0.0012$.

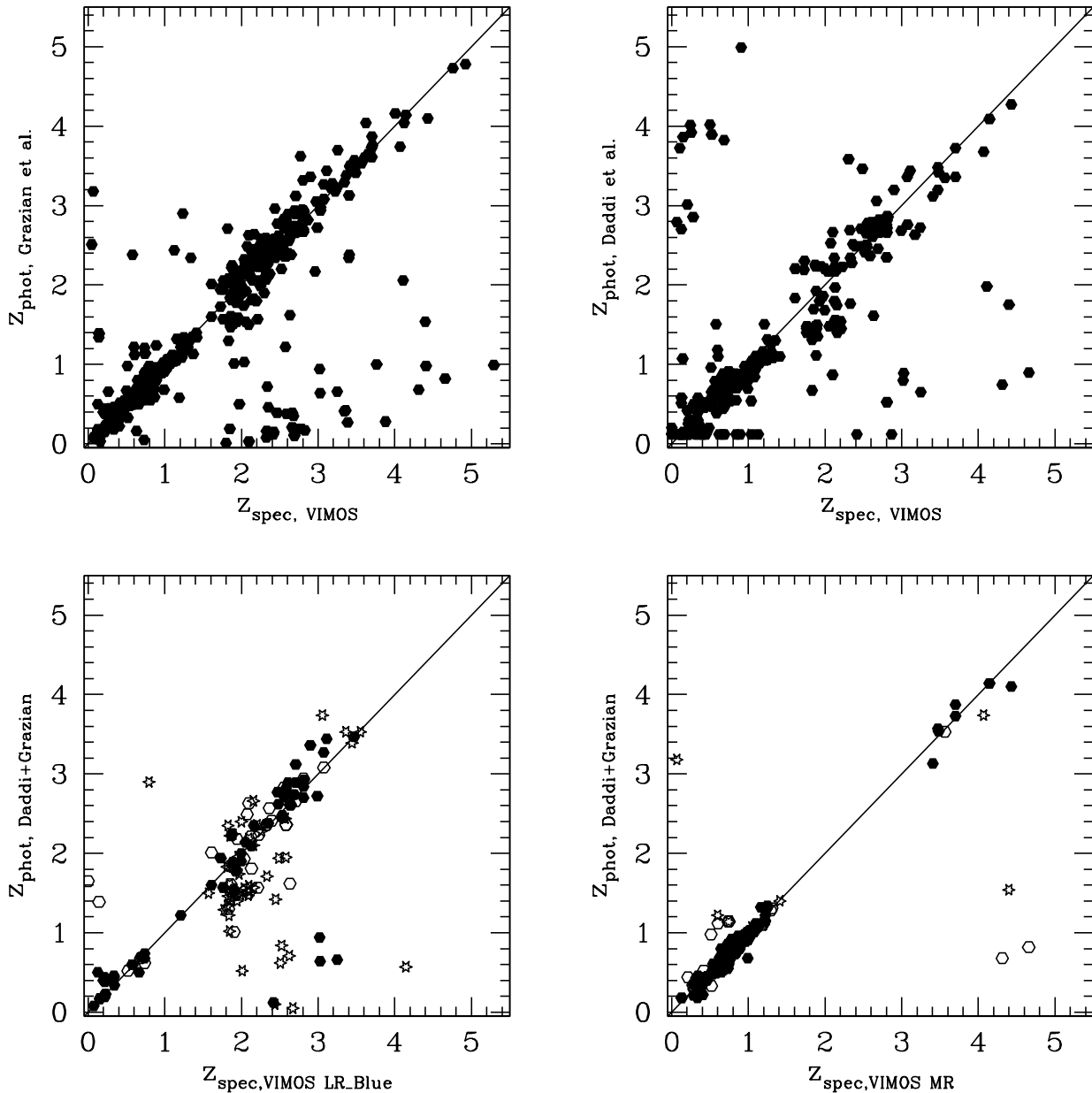


Fig. 5. z_{spec} versus z_{phot} . The two top panels show the comparison between the GOODS VIMOS (LR-Blue + MR) high quality z_{spec} and the GOODS-MUSIC z_{phot} of Grazian et al. 2006 (top left panel) and the GOODS z_{phot} of Daddi et al. (private communication, top right panel). In both cases there is a rather high percentage of discrepancies located in different regions of the diagram. If we compare the LR-Blue (bottom left panel) and the MR (the bottom right panel) z_{spec} only with z_{phot} , which are consistent within 3σ in the GOODS-MUSIC and GOODS catalogs, the agreement is much higher. In both bottom panels the filled circles are flag A z_{spec} , the empty circles are B flag z_{spec} and the stars are C flag z_{spec} .

5.2. Reliability of the redshifts - comparison with photometric redshift

An alternative way to assess the reliability of the redshifts is to compare the present results with accurate photometric redshifts. Photometric redshift determinations are inevitably

plagued by a rather high incidence of catastrophic failures and present biases depending on the redshift determination procedure applied. Thus, to overcome these problems, we use simultaneously two different photometric redshift catalogs: the GOODS-MUSIC catalog (Grazian et al. 2006) and a GOODS photometric redshift catalog (Daddi et al., private communica-

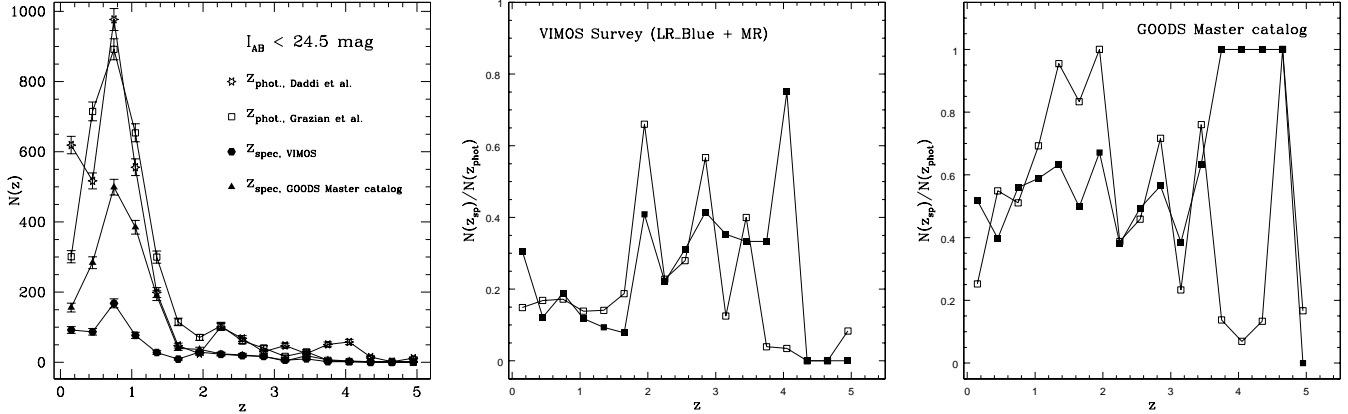


Fig. 6. Completeness level of the GOODS survey in the CDF-S. The left panel shows the coarse-grain redshift distribution of the z_{phot} catalogs considered for the comparison and the spectroscopic catalogs (GOODS VIMOS catalog and the GOODS master catalog containing all the available spectroscopic redshifts in the CDF-S). The central and the right panels show the spectroscopic completeness level of the GOODS VIMOS and the master catalogs, respectively, in several redshift bins. The completeness level is defined as the ratio $N(z_{spec})/N(z_{phot})$ in each redshift bin. In both panels the empty squares show the $N(z_{spec})/N(z_{phot})$ obtained from the GOODS-MUSIC catalog of Grazian et al.(2006) and the filled squares show the $N(z_{spec})/N(z_{phot})$ obtained from the GOODS catalog of Daddi et al.(private communication).

tion). The GOODS-MUSIC photometric redshifts are based on a high quality multiwavelength (from 0.3 to 8.0 μm) catalog, which includes accurate 'FSF-matched' ACS, *JHKs* ESO VLT, Spitzer IRAC and the first 3 h U-band VLT-VIMOS magnitudes. It is trained on the high quality GOODS-FORS2 and VVDS spectroscopic redshifts. The Daddi et al. (private communication) catalog is defined using a GOODS multi-color catalog including IRAC but with the exclusion of the VIMOS U-band, and trained using a whole set of high quality GOODS-FORS2, K20 and GMASS redshifts. For our purposes we have cross-correlated the two photometric redshift catalogs and created a high quality reference sample which includes only the objects with concordant GOODS-MUSIC and GOODS redshift estimations. We have calculated the σ of the $\Delta z = z_{Grazian} - z_{Daddi}$ distribution and identified the reference objects as those showing a $|\Delta z| < 3\sigma$. Fig. 4 shows the $z_{Grazian}$ versus z_{Daddi} . The filled circles lying within the 3σ lines (the solid lines in the figure) are those included in the reference photometric redshift sample and the empty circles are excluded from it. We have, then, compared this high quality reference z_{phot} sample with the VIMOS LR-Blue and MR spectroscopic catalog. Fig. 5 shows the result of the comparison. We define as "catastrophic" discrepancies the redshift determination with $|z_{spec} - z_{phot}| > 3\sigma$. We list below the results obtained for the LR-Blue survey:

- we find 150 common objects between the z_{phot} reference sample and the LR-Blue spectroscopic catalog. 65 of them have flag A, 34 have flag B and 51 have flag C
- there are 4 flag A "catastrophic" discrepancies: 1 of them is a secure Lyman break galaxies with strong $\text{Ly}\alpha$ in emission and well identified ultraviolet features and is not consistent with the $z_{phot} = 0.94$. In the remaining 3 spectra the emission line is identified as $\text{Ly}\alpha$ but it could be also an [OII]

as suggested by the z_{phot} . Thus 3 z_{spec} determinations out of 65 can be considered wrong, which confirms a confidence level of 95% in the low resolution flag A redshifts.

- we find 8 flag B discrepancies: 2 of them are secure low redshift emission line galaxies ([OII], $\text{H}\beta$ and [OIII] well identified). The remaining 6 spectra are solo-emission line ([OII] or $\text{Ly}\alpha$) spectra with few other low S/N features identified. If the line is identified differently ([OII] instead of $\text{Ly}\alpha$ or vice-versa) the resulting z_{spec} is consistent with z_{phot} . Thus, we consider these measurements wrong. The resulting confidence level is 82%
- there are 23 flag C z_{spec} which are not confirmed by the z_{phot} , which results in a confidence level about 55%

We list below the results obtained for the MR survey:

- we find 177 common objects between the z_{phot} reference sample and the MR spectroscopic catalog. 123 of them have flag A, 37 have flag B and 17 have flag C
- there are 2 flag A "catastrophic" discrepancies. Both cases are secure low redshift emission line galaxies ([OII], $\text{H}\beta$ and [OIII] well identified). Thus the confidence level of the MR A flag redshifts is confirmed to be 100%
- we find 6 flag B discrepancies: 2 of them are secure low redshift emission line galaxies. In the remaining 4 spectra, the emission line is located in the fringing region and could be misclassified. The resulting confidence level is 89%
- there are 4 flag C z_{spec} which are not confirmed by the z_{phot} , which results in a confidence level about 76%

5.3. The survey completeness

The main purpose of the two complementary GOODS-South redshift surveys, the FORS2 and VIMOS campaigns, is to provide a highly complete spectroscopic sample down to $i_{775} = 25$

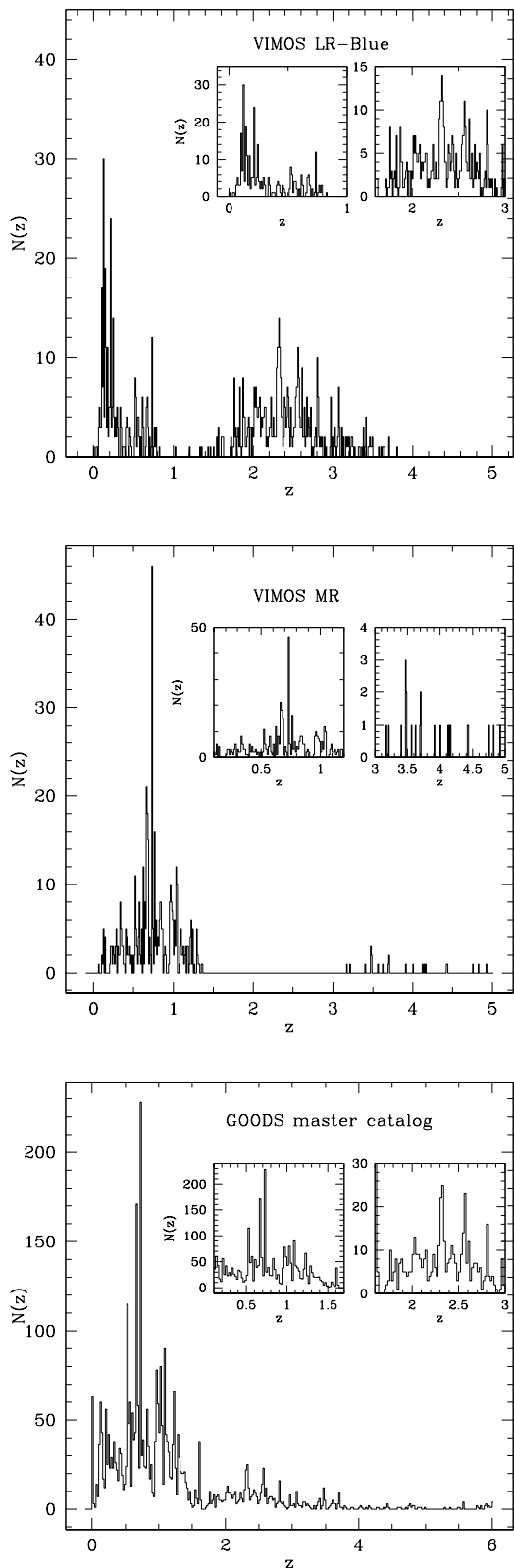


Fig. 7. Fine-grain redshift distribution of the available spectroscopic catalogs: the VIMOS LR-Blue catalog in the top panel, the VIMOS MR catalog in the central panel and the GOODS master catalog in the bottom panel. The smaller panels within the main frames show the distribution in the redshift region of particular interest.

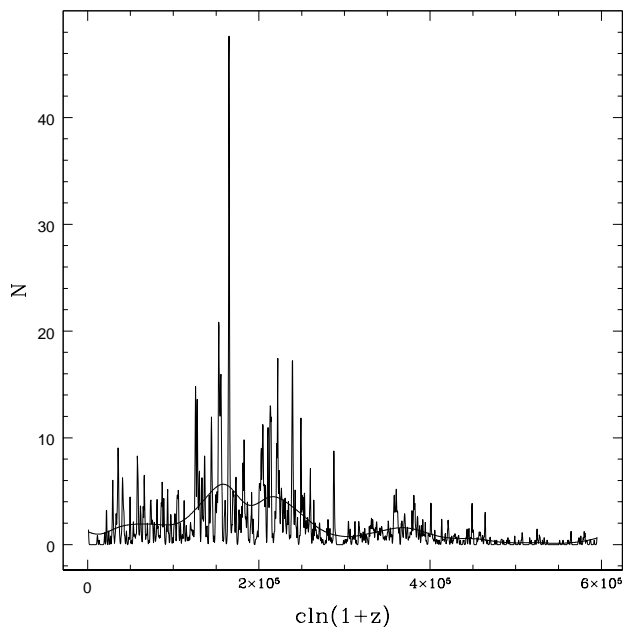


Fig. 8. Galaxy density in velocity space. The solid line is the background distribution obtained by smoothing the observed distribution with a Gaussian with $\sigma_C = 15000 \text{ km s}^{-1}$ (solid line). The galaxy distribution is recomputed using $\sigma_S = 300 \text{ km s}^{-1}$ (histogram).

mag. Thus, it is very important to know which is the real level of completeness reached so far after the completion of the whole FORS2 survey and 60% of the VIMOS survey. In principle, the selection function of a spectroscopic survey could be estimated by to the comparison with appropriate simulations able to reproduce the results of the applied target selection criteria. In the case of the FORS2 and VIMOS campaigns this is complicated by the fact that the selection criteria are not uniform throughout the survey. In fact, they have been tailored for each observing run in order to optimizing the survey success rate in terms of redshift estimation on the basis of partial results. To overcome this problem we use here a different approach. We compare our spectroscopic redshift catalog with a fairly complete photometric redshift catalog. As in the previous section we use two z_{phot} catalogs, the GOODS-MUSIC catalog and the GOODS catalog of Daddi et al. to take under control possible biases. The largest fraction of the GOODS-MUSIC sample is 90% complete at $z \sim 26$ or $K_s \sim 23.8$ mag (AB scale). In a similar way, the GOODS catalog of Daddi et al. includes all the GOODS sources with $K_s < 22$ mag (Vega scale). Since we are calculating the completeness level of our spectroscopic catalog in the ACS i band, we have checked that both z_{phot} catalogs are able to reproduce within the errors the observed number counts in the considered band down to the required magnitude limit ($i_{775} = 25$). As shown in the left panel of Fig. 6, both z_{phot} catalogs are able to reproduce the same coarse-grain redshift distribution within 3σ . The redshift bin is chosen to be $\delta z = 0.3$ very close to the 3σ uncertainty obtained in the comparison of the two z_{phot} catalogs. The same panel

shows also the coarse-grain redshift distribution of the VIMOS (LR-Blue+MR, the filled circles) survey and of the GOODS “master catalog”, namely the compilation of all high quality spectroscopic redshifts (GOODS FORS2 quality A and B, VIMOS LR-Blue+MR quality A and B, K20 quality 1, VVDS quality 3 and 4 and Szokoly et al. 2004 quality 3 and 2+ redshifts), cleaned of double observations. The completeness level in each redshift bin is calculated as the ratio $N(z_{spec})/N(z_{phot})$. The central panel of Fig. 6 shows the redshift-dependent completeness level of the whole GOODS-VIMOS survey, and the right panel shows the same results for the GOODS master catalog. The two z_{phot} catalogs provide consistent results within the error bars in both panels till redshift $z = 3.5$. The completeness level of the GOODS master catalog is rather high, $\sim 60\%$ till $z \sim 3.5$.

At higher redshift the discrepancy is larger than 3σ (the error bars are not shown in the central and right panels for clarity). This large discrepancy do not allows to draw any conclusion in this redshift range.

Table 2. Peaks detected in the master catalog redshift distributions, sorted by increasing redshift. The signal and background distribution are smoothed with $\sigma_S = 300\text{km s}^{-1}$ and $\sigma_B = 15000\text{km s}^{-1}$, respectively. Together with the mean redshift of each peak, the number of sources N within 1000km s^{-1} from the each peak and the type of LSS are also shown.

z	N	S/N	type
0.1241	37	> 5	groups
0.2190	19	> 5	sheet like
0.3393	18	> 5	sheet like
0.5269	26	> 5	sheet like
0.6741	49	> 5	filament
0.7355	174	> 5	cluster
0.9766	31	> 5	cluster
1.0310	21	> 5	sheet like
1.0990	45	> 5	cluster/group
1.2240	48	> 5	cluster/group
1.3060	13	> 5	cluster/group
1.6160	13	> 5	group
2.3160	8	> 4.5	sheet like
2.5600	7	> 4.5	sheet like

5.4. Redshift distribution and Large Scale Structure

Fig. 7 shows the fine-grin redshift distribution of the VIMOS LR-Blue (top panel), the VIMOS MR (the central panel) and the GOODS master spectroscopic catalog (the bottom panel). The smaller panels within each main panel show redshift regions of particular interest. Only the very high quality redshifts have been used for the analysis (flag A and B VIMOS and FORS2 redshift, flag 1 K20, flag 3 and 4 VVDS redshifts and flag 2 and 3 of Szokoly et al. 2004). To assess the significance of the observed large scale structures we follow a procedure suggested by Gilli et al. (2003) and similar to the one of Cohen et al. (1999). The sources are distributed in $V = c \ln(1 + z)$

rather than in redshift, since dV corresponds to local velocity variations granted the Hubble expansion. The observed distribution is then smoothed with a Gaussian with $\sigma_S = 300\text{km s}^{-1}$ (see fig. 8) to obtain the ‘signal’ distribution. Since there is no a priori knowledge of the ‘background’ distribution, we heavily smoothed the observed distribution with a Gaussian with $\sigma_B = 15000\text{km s}^{-1}$ and considered this as the background distribution. We then searched for possible redshift peaks in the signal distribution, computing for each of them the signal to noise ratio defined as $S/N = (S - B)/B^{1/2}$, where S is the number of sources in a velocity interval of fixed width $\Delta V = 2000\text{km s}^{-1}$ around the center of each peak candidate and B is the number of background sources in the same interval. Adopting the threshold $S/N \geq 5$ we find 14 peaks. In order to estimate the expected fraction of possibly “spurious” peaks arising from the background fluctuations, we have simulated 10^5 samples of the same size of the observed distribution and randomly extracted from the smoothed background distribution and applied our peak detection method to each simulated sample. With the adopted threshold, the average number of spurious peaks due to background fluctuations is 0.09. Of the simulated samples, 6.6% show one spurious peak, 0.3% show two spurious peaks, and only two simulation (out of 10^5) has three spurious peaks. None of the simulated samples have four or more spurious peaks. The 14 peaks detected in the described procedure are listed in Table 2, with the mean redshift of the peak the number of object (N) within 1000km s^{-1} from the peak, the SN threshold and a short description of the kind of large scale structure defined by visual inspection of the galaxy spatial distribution. We briefly compared our findings with previous works:

- the three clusters at 0.53, 0.67 and 0.73, already seen in the GOODS-FORS2 and K20 surveys are confirmed by the VIMOS redshifts. The peak at 0.077 seen in Gilli et al. is not detected in the master catalog. We do confirm the sheet-like structures observed at 0.219 in Gilli et al. (2003) and 0.339 (even if they observe a structure at marginally higher redshift $z=0.367$). An additional scale structure is visible at 0.1241. A cluster-like structure is also visible at 0.9766 as confirmed by an extended X-ray emission observed by Szokoly et al. (2004). We confirm the detection of the concentrated structures at $z=1,031,1,224,1.616$ already seen in K20 by Cimatti et al. (2003), in the X-ray sample by Gilli et al. (2003) and in the FORS2 sample by Vanzella et al. (2006). We observe additional significative peaks at $z=1.0990$ and 1.3060 as seen by Adami et al. (2005) and Vanzella et al. (2006).
- We note that other two peaks have been detected with a $S/N \sim 4.5$ at 2.316 and 2.560. The second one has been observed also by Gilli et al. (2003). In both cases the galaxy within 1000km s^{-1} from the peak occupy the whole GOODS region in a sheet-like structure. The probability to detect spurious peaks arising from the background distribution with a SN equal or greater than $SN \sim 4.5$ is about 10^{-3} .
- 124 galaxies are observed in the GOODS master sample in the redshift range $3 < z < 4$. No over-densities are confirmed in the considered redshift range.

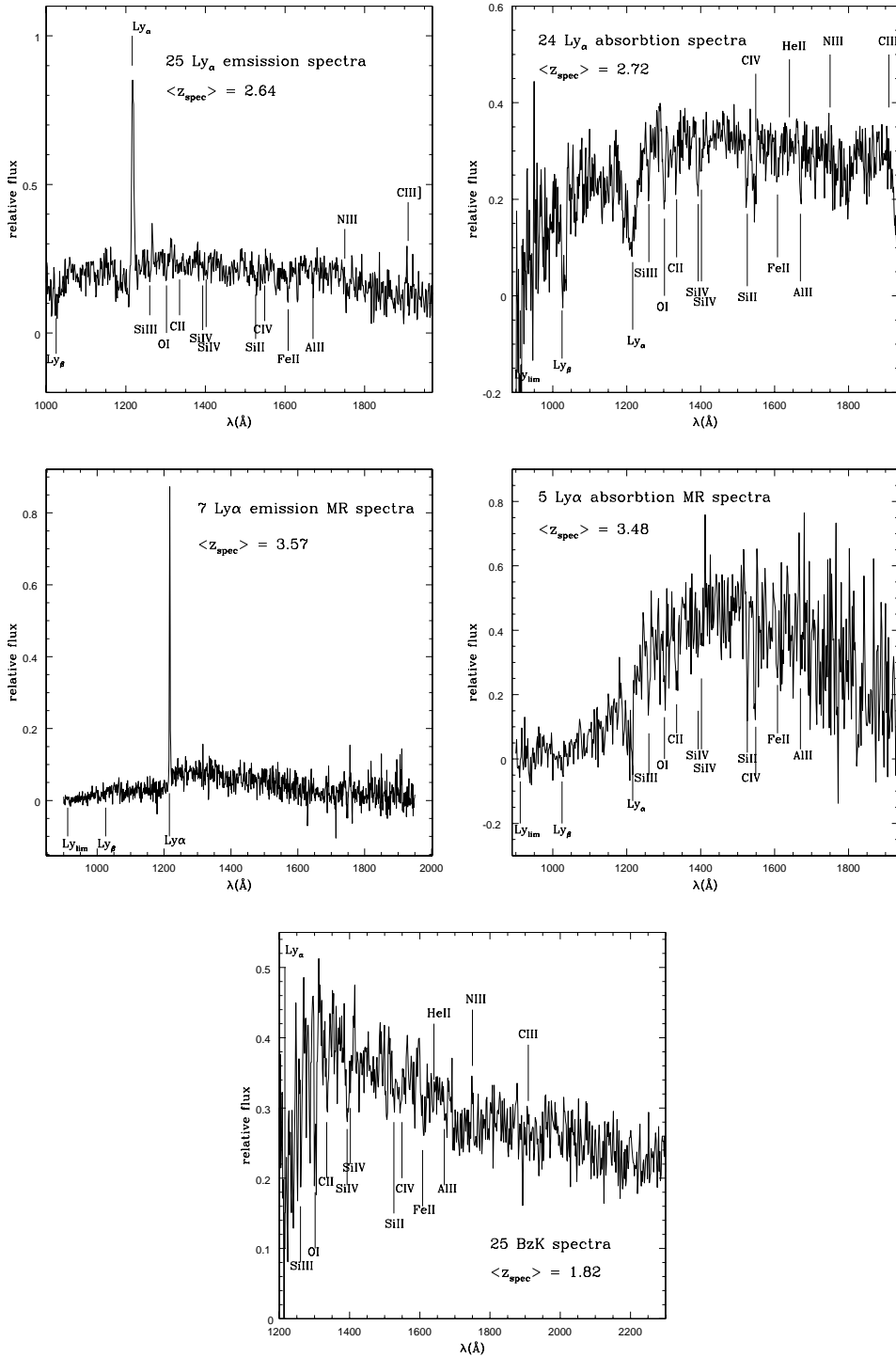


Fig. 9. Combined 1D spectra of high redshift galaxies in different redshift bins. The top panels show LBGs with the Ly α in emission (left panel) and in absorption (right panel) obtained with the LR-Blue grism at $z \sim 2.7$. The central panels show LBGs with the Ly α in emission (left panel) and in absorption (right panel) obtained with the MR grism at $z \sim 3.5$. The bottom panel shows the combined 1D spectrum of a BzK galaxy obtained with the LR-Blue grism at $z \sim 1.82$.

– 51 galaxies are observed in the GOODS master sample in the redshift range $4 < z < 5$ and 46 at $z > 5$. No overdensities are confirmed in the considered redshift range.

The composite spectra of such absorption and emission high redshift LBGs are shown in Fig. 9.

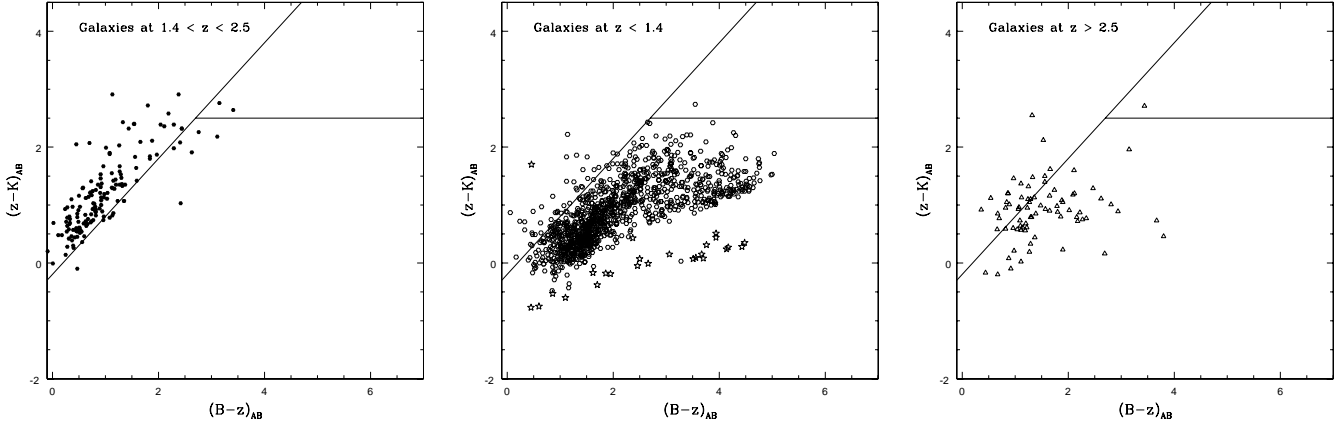


Fig. 10. BzK diagrams for the GOODS galaxies of the master catalog. The left panel shows the galaxies at $1.4 < z < 2.5$, the central panel shows the low redshift galaxies ($z < 1.4$) and the stars, and the right panel shows the galaxies at $z > 2.5$. In the central panel, the empty circles refer to the low redshift galaxies and the stars refer to the stars. The solid lines show the regions at $(z - K) - (B - z) > 0.2$ and $(z - K) - (B - z) < 0.2, B - z > 2.5$ where the star forming and passive BzK galaxies, respectively, lie.

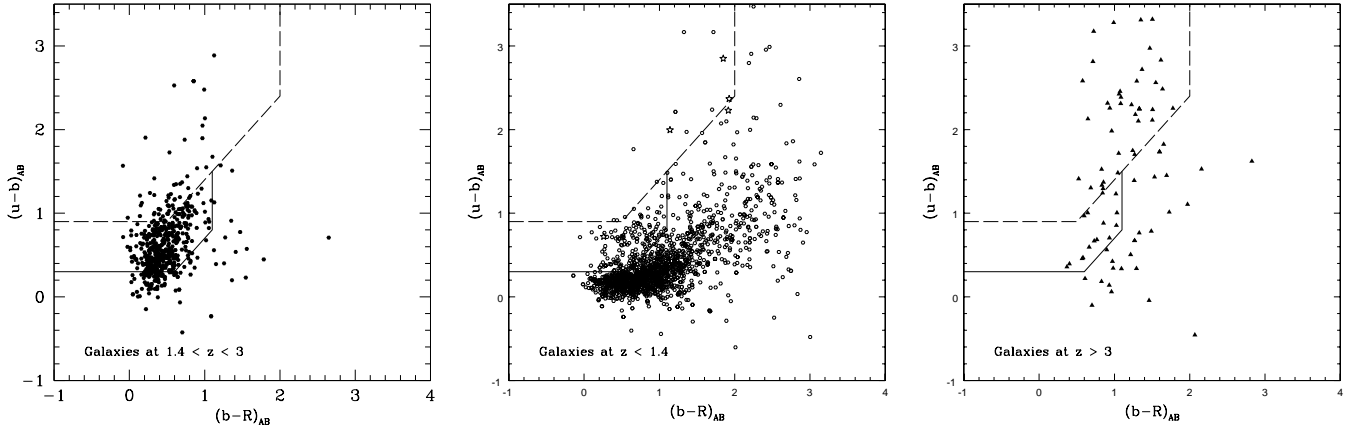


Fig. 11. $u-b-b-R$ color diagrams for the GOODS galaxies of the master catalog. The left panel shows the galaxies at $1.4 < z < 3$, the central panel shows the low redshift galaxies ($z < 1.4$), and the right panel shows the galaxies at $z > 3$. In the central panel, the empty circles refer to the low redshift galaxies and the stars refer to the stars. The region comprised between the solid and the dashed lines is the sub-U-dropout locus. The U-dropouts lie above the dashed line

6. Reliability of the photometric techniques for the selection of galaxies at $1 < z < 3$

Many photometric techniques have been proposed to select galaxies at high redshift, namely $z > 1.5$. Many of them (X-ray, BzK, 'sub'-U-dropouts, U, B and V-dropouts criteria) have been used to target for spectroscopy many of the CDF-S objects in different spectroscopic surveys. We have combined the results of all these surveys for creating a master catalog (see previous section), that reaches a high level of completeness ($> 50\%$) at $1.5 < z < 3.5$. The master catalog allows us to check the reliability of different photometric selection techniques by estimating their contamination due to low redshift galaxies and their completeness.

Fig. 10 shows the BzK diagram of Daddi et al. (2004), which aims to select galaxies at $z > 1.4$. The galaxy popula-

tion at $1.4 < z < 2.5$ (left panel), $z < 1.4$ (central panel) and $z > 2.5$ (right panel) have been showed in separated diagrams for clarity. The PSF-matched colors of the BzK catalog used in Daddi et al. (2007a, 2007b) have been used in the diagrams. The solid lines show the regions at $(z - K) - (B - z) > 0.2$ and $(z - K) - (B - z) < 0.2, B - z > 2.5$ where the star forming and passive BzK galaxies at $z > 1.4$, respectively, lie. $\sim 86\%$ of galaxies at $1.4 < z < 2.5$ lie in the expected BzK region. 14% of those are not classified as BzK and lie in the low redshift region. As shown in the central panel, the whole population (92%) of the galaxies at $z < 1.4$ populate the expected BzK region ($(z - K) - (B - z) < 0.2$ and $B - z < 2.5$) and only 8% of those are distributed in the other regions of the diagram. The galaxies at $z > 2.5$ can not be localized in a specific locus in the diagram. Only 27% of those higher redshift ob-

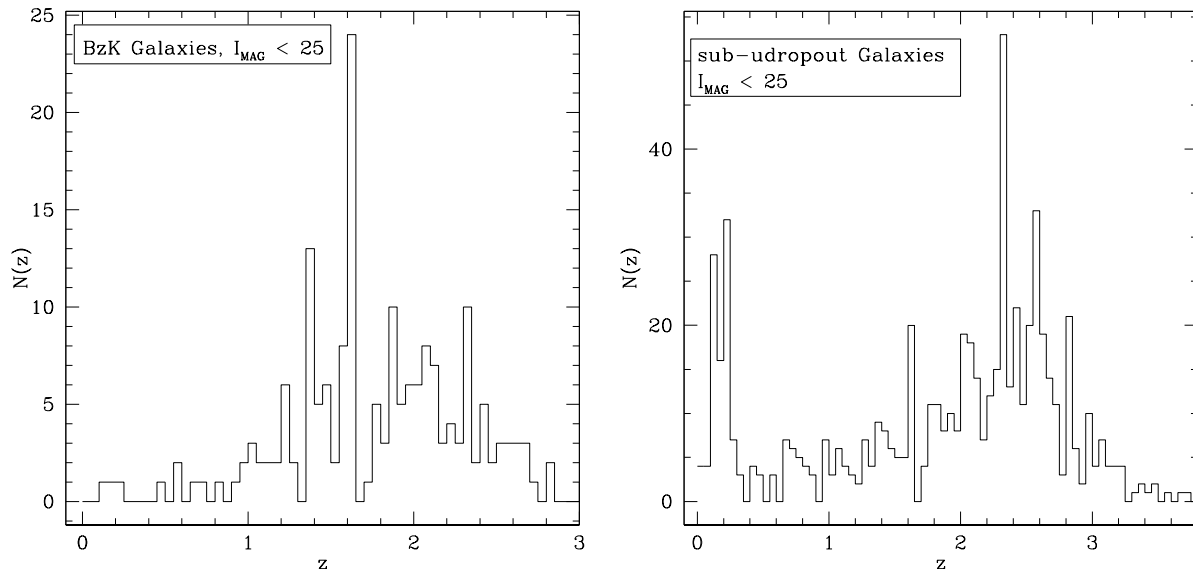


Fig. 12. Redshift distribution of the BzK selected (left panel) and sub-U-dropout (right panel) galaxies.

jects lie at $(z - K) - (B - z) > 0.2$ and the remaining 73% are located in the locus of the low redshift galaxies. This is expected because at $z > 2.5$ the Lyman forest starts to enter the B band, thus producing a reddening of the B-z color. To estimate the contamination due to low redshift galaxies in the BzK selection, we have distinguished the populations of BzK star forming ($(z - K) - (B - z) > 0.2$) and passive galaxies ($(z - K) - (B - z) < 0.2, B - z > 2.5$) from the low redshift objects at $(z - K) - (B - z) < 0.2$ and $B - z < 2.5$ and look for their redshift distributions. The star forming BzK population has the following composition: 67% of the sample lie at $1.4 < z < 2.5$, 10% at $z > 2.5$ and the contamination of low redshift galaxies is 23% (see also the left panel of fig. 12). In the BzK passive galaxy region there are only 2 galaxies. 2 of them are at $1.4 < z < 2.5$, one at $z > 2.5$ and one at low redshift. We performed this analysis by adopting different magnitude limit cuts ($I_{MAG} = 25$ mag to 23.5 mag), thus different completeness levels ($\sim 41\%$ to $\sim 55\%$). The results remain unchanged. This estimate is higher than the $\sim 8\%$ fraction of $z < 1.4$ galaxies found by Daddi et al. (2007). The difference is largely due to the fact that the latter work excluded from the analysis hard X-ray sources and blended galaxies.

We have used the same approach to estimate completeness and contamination of the sub-udrop-out selection criterion. The purpose is to select galaxies in the redshift window $1.4 < z < 3$. This criterion aims to be very similar to the BMBX selection method proposed by Adelberger et al. (2004). The BMBX selection method is based on selecting galaxies on the basis of their colors in the $U_n - G, G - R_s$ color color diagram. No U_nGR_s photometry is available for the CDF-S. So the $U - B$ and $B - R$ colors have been used to define similar color cuts (see Nonino et al. 2008 in preparation for more details). The sub-U-dropouts criteria are:

$$U - B > B - R - 0.3$$

$$B - R < 1.1$$

$$R > 23$$

and not meeting the standard U-dropout criterion. The U-dropout criteria are:

$$U - B > 0.9$$

$$U - B > B - R + 0.4$$

$$B - R < 2$$

$$R > 23$$

Fig. 11 shows the $u - b$ and $b - R$ color color diagram for the galaxy populations at $1.4 < z < 3$ (left panel), $z < 1.4$ (central panel) and $z > 3$ (right panel), respectively. The sub-U-dropout locus is located below the U-dropouts locus (thus, the name 'sub'-U-dropouts). It is enclosed within the solid and the dashed lines showed in the diagrams of fig. 11. The U-dropouts lie in the area enclosed by the dashed line. As showed in the left panel of the figure, most of the galaxies (80%) at $1.4 < z < 3$ lie in the locus of the sub-udrop-out region and 8% in the u-drop locus. Almost the whole population at $z < 1.4$ (92%) do not lie in the sub-U-dropouts and U-dropouts loci, as showed in the central panel. 58% of the population at $z > 3$ lie in the U-dropout region and 16% in the sub-U-dropout region (left panel). We have estimated the contamination of the sub-udropout criterion in analogous way to the BzK method. 72% of the sub-U-dropouts candidates at $R > 23$ turn out to be at $1.4 < z < 3$ with a contamination of 24% of low redshift objects ($z < 1.4$) and a remaining 4% of higher redshift objects ($z > 3$) (see also the right panel of fig. 12). The contamination by low redshift galaxies is similar to that of the BzK selection method and it is consistent with the results obtained by Adelberger et al. (2004). We have done the same exercise for the U-dropout (as defined above) and the B- and V-dropout selection method (as defined in Giavalisco et al. 2004). In all three cases the LBG technique provides galaxy samples in the desired redshift range with a

~ 80% completeness and a ~ 25% contamination by lower redshift galaxies.

7. Conclusions

In the framework of the Great Observatories Origins Deep Survey a large sample of galaxies in the Chandra Deep Field South has been spectroscopically targeted. A total of 3312 objects with $i_{775} \lesssim 25$ has been observed with the VIMOS spectrograph with the LR-Blue and MR grism at the ESO VLT providing 2137 redshift determinations. From a variety of diagnostics the measurement of the redshifts appears to be highly accurate (with a typical $\sigma_z = 0.001$) and reliable (with an estimated rate of catastrophic misidentification at most few percent). The spectroscopic coverage of the CDF-S obtained by combining the VIMOS spectroscopic sample with the available redshifts in the literature is very high, ~ 60% up to redshift $z \sim 3.5$. It is more uncertain above this limit. The compilation of the redshifts presented in this paper and all redshift determinations available in the literature have been used to test the accuracy of the BzK, sub-U-dropout and drop-outs selection techniques. We showed that any of these methods allows to create high redshift galaxy samples with a contamination of ~ 25% of low redshift sources and a completeness level of 80%. The same 'master' catalog has been used also to identify several large scale structures in the GOODS region.

The reduced spectra and the derived redshifts are released to the community (<http://www.eso.org/science/goods/>). They constitute an essential contribution to reach the scientific goals of GOODS, providing the time coordinate needed to delineate the evolution of galaxy properties, morphologies, and star formation and to underhand the galaxy mass assembly.

Acknowledgements. We are grateful to the ESO staff in Paranal and Garching who greatly helped in the development of this programme. We would like to thank Martino Romaniello and Carlo Izzo for many stimulating discussions and for the help in reducing the VIMOS data. We would like to thank also Remco Slijkhuis and Joerg Retzlaff for their work on VIMOS/GOODS release.

References

- Adami, C.; Mazure, A.; Ilbert, O. 2005, A&A, 443, 805
- Adelberger, K. L., Steidel, C. C., Shapley, A. E. et al. 2004, ApJ, 607, 226
- Bottini, D.; Garilli, B.; Maccagni, et al. 2005, PASP, 117, 996
- Cimatti, A., Mignoli, M., Daddi, E., et al. 2002, A&A, 392, 395
- Cohen J. G., Blandford, R., Hogg, D. W., et al. 1999, ApJ, 512,30
- Dickinson et al. 2003, in the proceedings of the ESO/USM Workshop "The Mass of Galaxies at Low and High Redshift" (Venice, Italy, October 2001), eds. R. Bender and A. Renzini, astro-ph/0204213
- Dickinson, M., et al., 2004, ApJ, 99, 122
- Daddi, E.; Cimatti, A.; Renzini, A. 2004, et al., ApJ, 617, 746
- Daddi, E., Alexander, D. M., Dickinson, M. et al., 2007, ApJ, 670,173
- Daddi, E., Dickinson, M., Morrison, G.2007, et al, ApJ, 670, 156
- Giacconi, R., Zirm, A., Wang, J. et al. 2002, ApJS, 139, 369
- Giavalisco, M., Ferguson, H. C., Koekemoer, A. M., et al. 2004, ApJ, 600, L93
- Gilli, R., Cimatti, A., Daddi, E. et al. 2003, ApJ, 592, 721
- Grazian, A., Fontana, A., de Santis, C. et al., 2006, A&A, 449, 951
- Horne, K. 1986, PASP, 98, 609
- Le Fevre, O., Vettolani, G., Maccagni, D., et al. 2003, SPIE, 4834, 173
- Le Fevre, O., Vettolani, G., Paltani, S., et al. to A&A, 428, 1043
- Lehmer, B. D., Brandt, W. N., Alexander, D. M., et al. 2005, ApJS, 161, 21
- Renzini et al. 2002, in the proceedings of the ESO/USM Workshop "The Mass of Galaxies at Low and High Redshift" (Venice, Italy, October 2001), eds. R. Bender and A. Renzini
- Scodreggio, M., Franzetti, P.; Garilli, B., et al. 2005, PASP, 117, 1284
- Szokoly, G., P., Bergeron, J., Hasinger, G.et al. 2004, ApJS, 155, 271
- Vanzella E., Cristiani, S., Dickinson, M., Kuntschner, H., Moustakas, L. A., Nonino, M., Rosati, P., Stern, D., Cesarsky, C., Ettori, S et al. 2005 A&A, 434, 53
- Vanzella E., Cristiani, S., Dickinson, M., Kuntschner, H., Nonino, M., Rettura, A., Rosati, P.; Vernet, J., Cesarsky, C., Ferguson, H. C. et al. 2006, A&A 454, 423
- Vanzella E., Cristiani, S.; Dickinson, M.; Giavalisco, M.; Kuntschner, H.; Haase, J.; Nonino, M.; Rosati, P.; Cesarsky, C.; Ferguson, H. C. et al.2008, A&A, 478, 83
- Vogt, P.N., et al. 1996, ApJ, 465, L15
- Vogt, P.N., et al. 1996, ApJ, 479, L121
- Warmels, R.H.: 1991, "The ESO-MIDAS System", in Astronomical Data Analysis Software and Systems I , PASP Conf. Series, Vol. 25, p. 115.

This figure "mrcoverage.jpg" is available in "jpg" format from:

<http://arxiv.org/ps/0802.2930v1>

This figure "zg_zd.jpg" is available in "jpg" format from:

<http://arxiv.org/ps/0802.2930v1>